KINEMATIC ANALYSIS AND OPTIMIZATION OF OPERATIONAL POSITION FOR SPECIALIZED ROBOTS USED FOR INSPECTING THE UNDERBOUND SURFACE OF BRIDGES

Van Luan Bui[1], Van Duong Le[1], Van Tram Bui[2]*, Van Hung Nguyen[3]

[1]*Military Technical Academy, Vietnam*

[2]*University of Transport Technology, Vietnam*

[3]*Institute of Mechanics Automation Measurement in Institute of Transportation Science and Technology, Vietnam*

*Corresponding author: trambv@utt.edu.vn

(Received: February 02, 2026; Revised: March 15, 2026; Accepted: March 24, 2026)

DOI: 10.31130/ud-jst.2026.24(3).080E

Abstract - Specialized mobile robots for under-bridge inspection and maintenance play a crucial role in ensuring the safety and operational reliability of transportation infrastructure. This paper focuses on kinematic analysis and the optimization of operational positioning to enhance equipment efficiency. First, a kinematic model is developed based on the Denavit–Hartenberg (D-H) matrix method, enabling the accurate determination of the workspace envelope and the effective working radius. Based on these kinematic characteristics and optimization theory, the study proposes an algorithm for optimizing the base vehicle's stopping positions, subject to strict geometric constraints regarding surface coverage and safe overlap margins. Simulation results demonstrate that the proposed approach identifies an optimal step size that guarantees 100% accessibility to the bridge underside while minimizing the number of vehicle stops, thereby significantly improving operational efficiency.

Key words - Kinematics; under-bridge inspection vehicle; working envelope; operational optimization; vehicle step size; D-H parameters.

1. Introduction

Throughout their service life, road bridge structures inevitably undergo degradation due to the combined effects of traffic loads, harsh environmental conditions, and material aging [1]. Periodic inspection plays a decisive role in the early detection of structural defects, thereby ensuring structural integrity and extending the service life of the infrastructure. However, accessing the underside of bridge decks and girder systems remains a significant challenge due to confined working spaces and stringent occupational safety requirements [2].

Traditional methods, such as erecting scaffolding or utilizing manual rope-hanging systems, often exhibit major limitations regarding time, labor costs, and high potential safety risks [3]. In recent years, the trend of applying intelligent robotics in structural inspection has made significant strides, moving toward autonomous systems to optimize operational workflows [4], [5]. Although solutions using Unmanned Aerial Vehicles (UAVs) or cable-climbing robots have been extensively researched [6], [7], specialized manipulator units mounted on base vehicles maintain a superior advantage in terms of stability and load-carrying capacity for complex maintenance tasks [8].

In Vietnam, importing these specialized vehicles involves substantial investment costs, leading to an urgent need for research and mastery of "Made in Vietnam" bridge inspection equipment technologies to reduce costs and gain operational autonomy. One of the most critical links for the effective operation of these devices is the precise analysis of the manipulator's kinematic characteristics [9], [10]. Developing a kinematic model not only helps define the workspace envelope but also serves as vital input data for control algorithms and ensuring positional accuracy [11]. Previous studies in [12-15] also applied kinematic analysis for computational design, torque-controller development, and velocity-level control of various robotic systems.

However, most current studies focus primarily on mechanical design or pure kinematic analysis without delving deeply into the optimization of operational positioning. In practice, determining the stopping positions of the base vehicle often relies on empirical intuition, which easily leads to missing inspection points or time wastage due to excessive scan overlap. To address this issue, this paper presents a study on the kinematic modeling of a multi-link under-bridge inspection manipulator and proposes an algorithm to optimize the base vehicle's step size. The novelty of this research lies in the integration of workspace profile analysis with a staggered scanning strategy to completely eliminate "dead zones" under the bridge deck, thereby enhancing the operational efficiency of the equipment.

2. System structure and computational basis

2.1. Structural Configuration and Operating Principles

This paper investigates the kinematic characteristics of an under-bridge inspection device manufactured in Vietnam, as described in Figure 1.

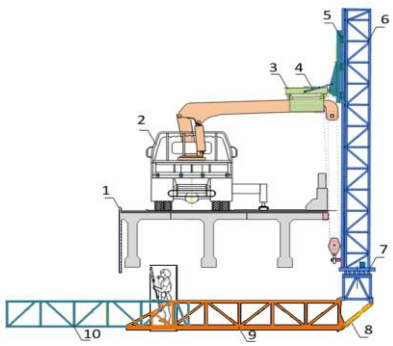

Figure 1. *The structural configuration of the device*

The under-bridge inspection device investigated in this study is a specialized manipulator system integrated onto a mobile base vehicle. The structural assembly comprises key components: a vertical frame (6) for depth access, a working platform (9) for operators, and an extendable section (10) to maximize reach. The deployment process follows a 6-step sequence, transitioning the system from a folded transport state to a fully extended configuration beneath the bridge deck.

The combination of these structural assemblies creates a complete system that allows the device to safely and flexibly access hard-to-reach areas on the underside of the bridge, while ensuring operational efficiency and reliability during inspection tasks.

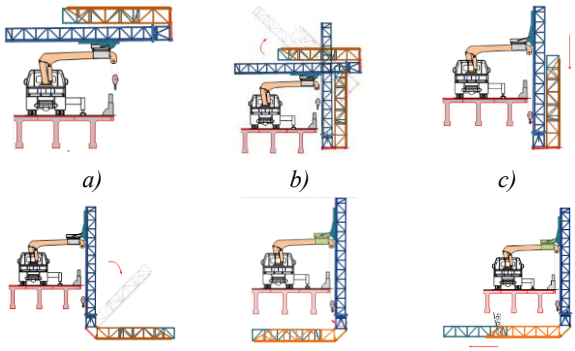

Figure 2. *Working Principles of the Device*

The operating principle of the device is carried out sequentially through the following steps (operations), as illustrated in Figure 2.

Step 1: The working assembly of the device is transported to the construction site using the base vehicle (truck crane). The working assembly is then mounted onto the base vehicle, and the device is positioned to prepare for subsequent operations (Figure 2a).

Step 2: The vertical frame, together with the working platform and the extension platform, is raised to a 90-degree position, perpendicular to the bridge deck (Figure 2b). This operation is performed by hydraulic cylinders connecting the vertical frame to the conversion module. The conversion module is fixed to the crane boom of the base vehicle.

Step 3: The vertical frame, along with the working platform and the extension platform, is lowered to the required depth (Figure 2c). This operation is performed using a pulley system driven by the suspension cable.

Step 4: The working platform and the extension platform are deployed perpendicular to the vertical frame (Figure 2d). This operation is actuated by two hydraulic cylinders connecting the platform to the vertical frame.

Step 5: The working platform and the extension platform are rotated beneath the bridge deck (Figure 2e). This operation is executed by the platform rotation mechanism driven by a hydraulic motor mounted under the working platform.

Step 6: The extension platform is extended to the required position (Figure 2f). This operation is performed using a chain-driven mechanism powered by a hydraulic motor.

After completing the above six steps, the operator moves onto the main platform and the extension platform through the vertical frame to carry out inspection or maintenance tasks. To inspect additional locations within the same working bay, the base vehicle is driven from one inspection position to another at a speed of approximately 5 km/h. The retraction process of the working assembly is performed in the reverse order, from Step 5 back to Step 1.

The main operating parameters of the under-bridge inspection device are presented in Table 1. These parameters describe the working dimensions, load-carrying capacity, and motion ranges of the working platform, serving as essential inputs for the development of the kinematic model and for evaluating the device's accessibility performance.

Table 1. *Main Operating Parameters of the Device*

Parameter	Value	Unit
Working platform width	0.8	m
Working platform length	7.0	m
Maximum allowable load on the working platform	200	kg
Platform rotation capability	180	Deg
Platform lifting (folding) capability	90	Deg

2.2. Kinematic Modeling

2.2.1. Modeling Assumptions

To facilitate precise control and workspace analysis, the device is modeled as a kinematic chain consisting of six links.

The links are illustrated in Figure 3.

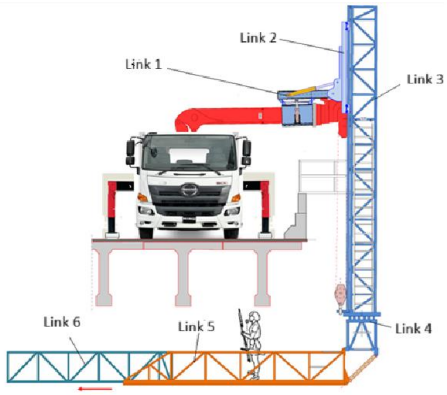

Figure 3. *Cylinder Working Priciple*

Modeling Assumptions: The links are considered rigid bodies interconnected by revolute and prismatic joints.

D-H Parameters: Reference frames are assigned to each link according to the Denavit-Hartenberg (D-H) convention. The geometric transformations between consecutive links are defined by four parameters: link length (a_i), link offset (d_i), twist angle (α_i), and joint angle (θ_i).

Jacobian Matrix: The relationship between joint velocities and end-effector velocities is established through the geometric Jacobian matrix (J). This matrix is essential for evaluating the system's dexterity and identifying potential singularities.

Based on the structural configuration and working principles of the device presented above, the kinematic diagram of the system is developed as shown in Figure 4.

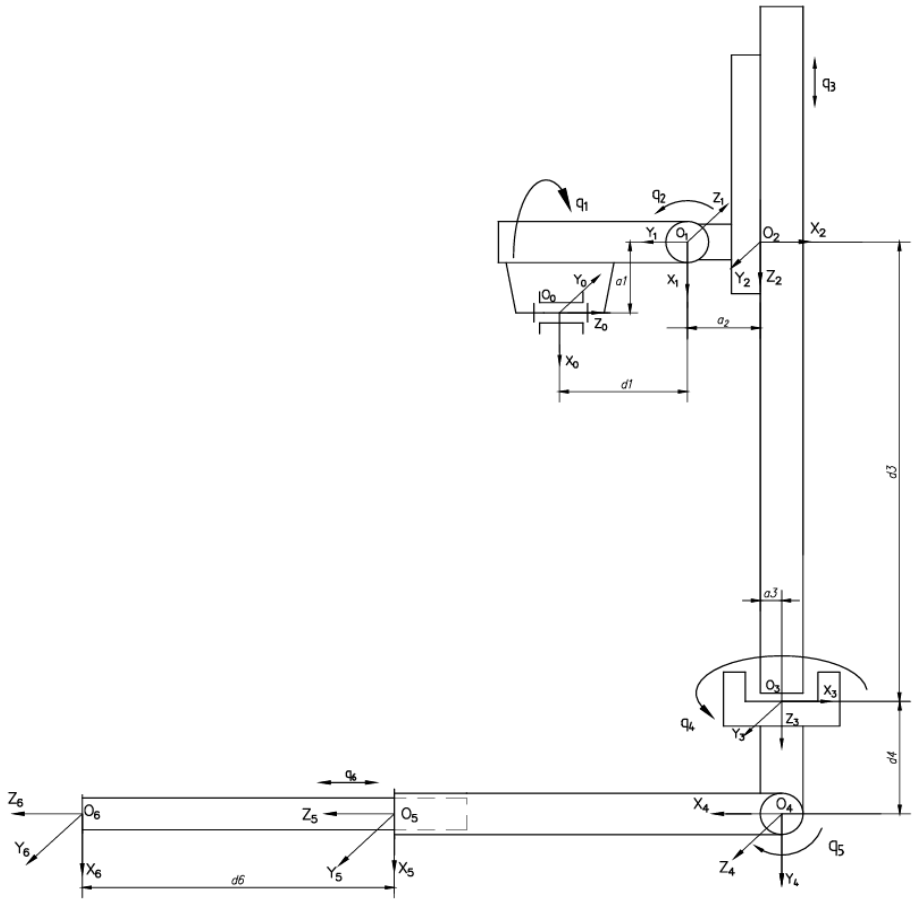

Figure 4. *Kinematic schematic of the under-bridge inspection device*

2.2.2. D-H parameters

We choose the coordinate frames as shown in Figure 4. The algorithm presented in the D–H convention is used to assign the proper coordinate frames for the device, and the corresponding parameters are listed in Table 2.

Table 2. *Device D-H Table*

i	θ_i	d_i	a_i	α_i	Joint variable
1	q_1	0,577	0,285	-90^0	q_1
2	q_2	0	0,384	-90^0	q_2
3	0	d_3	0,30	0^0	d_3
4	q_4	0,6	0	90^0	q_4
5	q_5	0	0	90^0	q_5
6	0	d_6	0	0^0	d_6

The generalized coordinates used to determine the configuration of the mechanism are defined according to the Denavit–Hartenberg method, in which:

q_1: Rotation angle of link 1 (base link) about the O_0Z_0 axis at joint O_0;

q_2: Rotation angle of the boom about the O_1Z_1 axis at joint O_1;

q_3: Translational displacement of link 3 along the O_2Z_2 axis of link 2;

q_4: Rotation angle of the platform-rotation unit about the O_3Z_3 axis at joint O_3;

q_5: Rotation angle of link 5 (main working platform) about the O_4Z_4 axis at joint O_4;

$q_6 = d_6$: Translational displacement of link 6 along the O_5Z_5 axis of link 5.

2.2.3. Geometric jacobian

Based on the proposed configuration, the mathematical formulas used to describe the system are as follows.

In this paper, we discuss Differential Kinematics. The goal of differential kinematics is to determine the relationship between the joint velocities and the linear and angular velocities of the end-effector. This mapping is represented by a matrix called the geometric Jacobian, which depends on the current configuration of the manipulator.

In general, the linear velocity $\dot{p}$ and the angular velocity ω of the end-effector can be expressed as a function of the joint velocities $\dot{q}$:

$$\begin{bmatrix} \dot{p} \\ \omega \end{bmatrix} = J(q)\,\dot{q} \tag{1}$$

Where:

$\dot{p}$: is the linear velocity vector of the end-effector.

ω: is the angular velocity vector of the end-effector.

$J(q)$: is the $(6 \times n)$ geometric Jacobian matrix.

$\dot{q}$: is the joint velocity vector.

The $(6 \times n)$ matrix J is the geometric Jacobian of the manipulator, which is typically a function of the joint variables.

From the Denavit–Hartenberg transformation matrices.

We obtain the 4×4 transformation matrices $\boldsymbol{H}_i$ $i = 1, 2, \ldots, 6$ that convert the coordinates of a point from the coordinate frame of link to link $(i-1)$ $x_{i-1}y_{i-1}z_{i-1}$ in the following form:

$$ {}^{i-1}\boldsymbol{H}_i = \begin{bmatrix} \cos\theta_i & -\sin\theta_i \cos\alpha_i & \sin\theta_i \sin\alpha_i & a_i \cos\theta_i \\ \sin\theta_i & \cos\theta_i \cos\alpha_i & -\cos\theta_i \sin\alpha_i & a_i \sin\theta_i \\ 0 & \sin\alpha_i & \cos\alpha_i & d_i \\ 0 & 0 & 0 & 1 \end{bmatrix} \quad (2) $$

The D-H parameters are defined as follows:

θ_i: The angle of rotation about the Z_{i-1} axis to align the X_{i-1} axis with the X_i axis.

d_i: The translation distance along the Z_{i-1} axis from the X_{i-1} axis to the X_i axis.

a_i: The translation distance along the X_i axis from the Z_{i-1} axis to the Z_i axis.

α_i: The angle of rotation about the X_i axis to align the Z_{i-1} axis with the Z_i axis.

The transformation matrices D_i between the base coordinate frame x_0, y_0, z_0 and link i x_i, y_i, z_i are given as follows:

$$ \boldsymbol{D}_i = \prod_{k=1}^{i} \boldsymbol{H}_k \quad (3) $$

The transformation matrices have the following form:

$$ \mathbf{D}_n = \begin{bmatrix} \mathbf{A}_n & \mathbf{r}_E^{(0)} \\ \mathbf{0}^T & 1 \end{bmatrix} \quad (4) $$

Where A_n is the 3×3 direction cosine matrix describing the orientation of the end link (link n) in the base coordinate frame; and $r_E^{(0)}$ is the 3×1 position vector specifying the coordinates of the end-effector.

By extracting the 3×3 rotational submatrix from the transformation matrix, we obtain the rotation matrix of link i and the position vector of the origin of link i's coordinate frame:

$$ A_i^O, r_{O_i}^O, \quad (5) $$

The general Jacobian matrix represents the relationship between the joint velocities and the linear and angular velocities of the end-effector:

The differential kinematic equation of the end of link 6

$$ \begin{bmatrix} \dot{r}_6 \\ \omega_6 \end{bmatrix} = \begin{bmatrix} J_\omega \\ J_\omega \end{bmatrix} \dot{q} \quad (6) $$

$$ \dot{r}_6 = J_v \dot{q} \; \omega_6 = J_\omega \dot{q} \quad (7) $$

We showed that the jacobian matrice can be shown as $(6 \text{ x } n)$ matrices. J can be partitioned into $(3 \text{ x } 1)$ column vectors. In these arms, the J matrices are $(6 \text{ x } 6)$. And can be shown as:

$$ J = \begin{bmatrix} J_{v,1} & J_{v,2} & J_{v,3} & J_{v,4} & J_{v,5} & J_{v,6} \\ J_{\omega,1} & J_{\omega,2} & J_{\omega,3} & J_{\omega,4} & J_{\omega,5} & J_{\omega,6} \end{bmatrix} \quad (8) $$

Where:

J_v: the linear Jacobian matrix, determined as

$$ J_{v,i} = \mathrm{z}_{i-1} \times (\mathrm{r}_6 - \mathrm{r}_{i-1}); \quad (9) $$

J_ω: the angular Jacobian matrix, determined as

$$ J_{\omega,i} = \mathrm{z}_{i-1} \quad \text{for revolute joints,} \quad (10) $$

$$ J_{\omega,i} = 0 \quad \text{for prismatic joints.} \quad (11) $$

The z-axis of link $i-1$ corresponds to the third column of the rotation matrix.

Where i= 1: 6 and $Z_0 = [0 \quad 0 \quad 1]^T$ allows selecting the third desired column.

2.2.4. Simulation results and workspace analysis

Based on the kinematic model and the Denavit–Hartenberg parameters established in the previous section, the workspace of the inspection device was determined through a systematic trajectory sweep simulation. The simulation process visualizes the actual operational envelope and verifies the accessibility of the manipulator mechanism. The resulting workspace is illustrated in Figure 5.

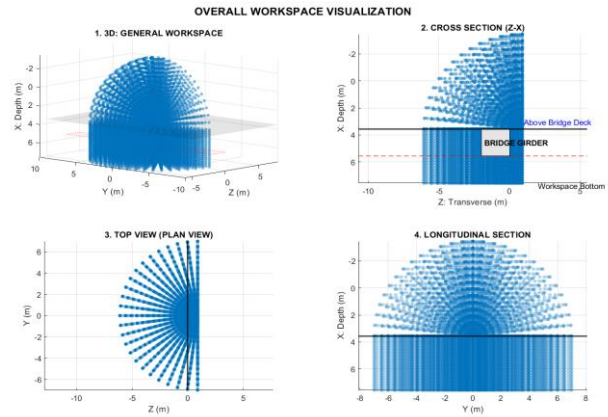

Figure 5. *Workspace of the extension platform endpoint*

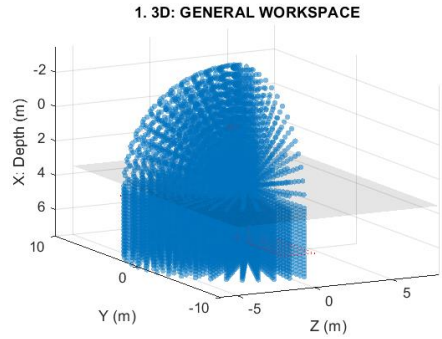

Figure 6. *3D General View*

The 3D simulation reveals that the total workspace forms a "cylindrical sector" or "fan-shaped volume". This geometry confirms that the combination of the rotational joint (q_4) and the translational telescopic arm d_6 allows the platform to effectively cover a vast volume beneath the bridge deck, ensuring access to complex structural components.

The projection on the vertical plane demonstrates the device's capability to reach the required depth while maintaining safety clearances. The theoretical workspace

(the set of blue points) completely encompasses the target "Bridge Girder" area. The red dashed line represents the minimum safe depth limit that the device needs to achieve, which corresponds to the underside surface of the bridge. The black line indicates the bridge deck surface; although the device does not operate in this area in reality, it is included in the simulation to provide the most comprehensive visual representation of the device's inspection zones and overall configuration.

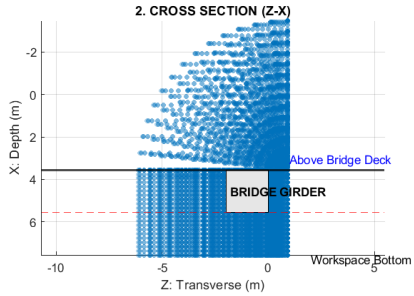

Figure 7. *Cross-sectional View (X-Z Plane)*

This is the most critical projection for operational strategy planning. The simulation results clearly depict the fan-shaped coverage generated by the rotational angles of the device's links and joints.

From this profile in Figure 8, the maximum effective working radius (R_{eff}) is determined to be approximately 6.0 m. This is the prerequisite input parameter for the vehicle step size optimization problem.

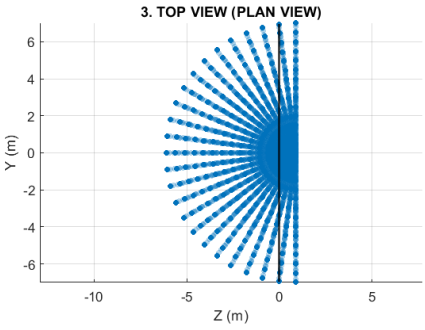

Figure 8. *Plan View (Y-Z Plane)*

The radial lines represent the extension range of the telescopic platform, highlighting the existence of inherent "dead zones" at the far corners of the rectangular bridge deck. This specific geometric characteristic serves as the scientific basis for the necessity of the "Staggered Scanning Strategy," which will be proposed in the subsequent section to eliminate these blind spots.

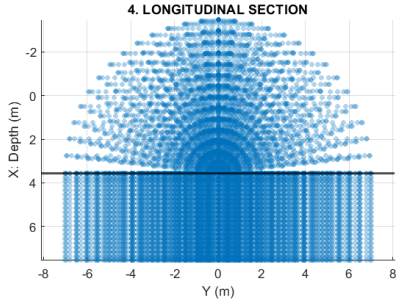

Figure 9. *Longitudinal View (X-Y Plane)*

The projection along the bridge length shows a dense and uniform distribution of reachability. The symmetric arc shape confirms the stability of the mechanism and its ability to maintain a consistent working depth across the entire rotational range.

3. Operational position optimization

The objective of the optimization problem is to determine the vehicle stopping positions and the moving step size (ΔL) so that the device can cover 100% of the under-bridge surface area with the minimum number of stops. The problem is formulated based on strict geometric constraints regarding reachability and safety.

3.1. Workspace Analysis and "Dead Zones" Identification

Simulation results reveal that the workspace of the extension platform endpoint forms a fan-shaped volume. Based on this profile, the maximum effective working radius (R_{eff}) is determined to be approximately 6.0 m. A critical finding is the geometric mismatch between the circular scanning trajectory and the rectangular bridge girder, which inherently creates "dead zones" (blind spots) at the corners of each scan.

Consider a case study where the bridge width equals the effective working radius ($B = R_{eff} = 6.0m$).

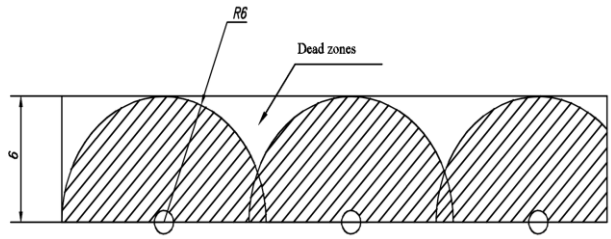

Figure 10. *Illustration of dead zones during single-sided longitudinal movement*

In the intersection area between two consecutive scans, curvilinear triangular zones emerge adjacent to the far edge of the bridge, which remain inaccessible to the operator.

For wide bridges ($R_{eff} < B < 2R_{eff} = 12m$), conducting an inspection from both sides is mandatory. However, if the symmetric parallel positioning method is applied, "diamond-shaped dead zones" will emerge along the longitudinal centerline of the bridge.

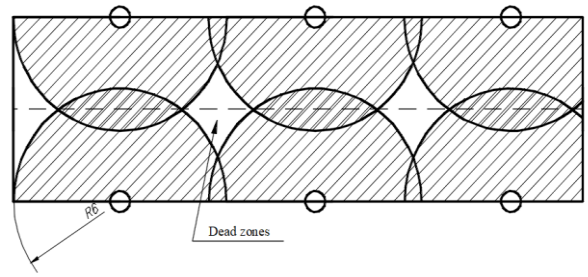

Figure 11. *Illustration of dead zones during symmetric parallel positioning*

Consequently, it is essential to develop a mathematical model to calculate a rational vehicle step size (ΔL) and implement a two-sided staggered scanning strategy to eliminate these dead zones.

3.2. Two-sided Staggered Scanning Strategy

To concretize the staggered scanning strategy, a geometric model is developed based on the interaction between the trajectories of the two opposing lanes. As illustrated in Figure [12], the vehicle stopping positions on the two lanes are phase-shifted (staggered) by exactly half a step size ($\frac{\Delta L}{2}$). The critical state of the optimization problem is identified at Point M – the convergence intersection between the workspace boundaries of the first lane (the two lower arcs) and the apex of the arc from the second lane (the upper arc). At this specific point, the condition for covering the bridge underside is strictly satisfied. Consequently, the coordinates of Point M serve as the binding constraint to establish the equation for determining the maximum step size ΔL as follows:

Determination of the "Weakest Point" of Lane 1 (The Valley)

When the vehicle moves along Lane 1 with a step size ΔL, the coverage area consists of a series of intersecting circles. The deepest indentation point (representing the largest geometric gap) is located exactly at the midpoint of the step ($x = \frac{\Delta L}{2}$). At this specific point, the maximum lateral reach of Lane 1 decreases to its minimum value:

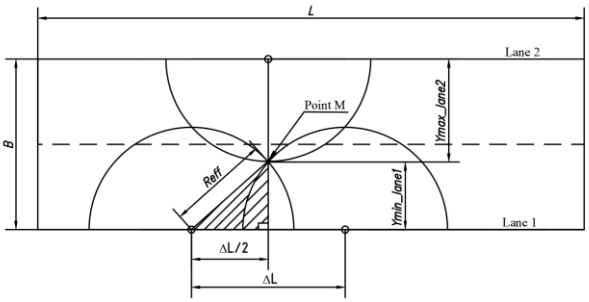

Figure 12. *Illustration of dead zones during single-sided longitudinal movement*

At Point M, as illustrated in Figure 12, the lateral reach (transverse reach) of the device in Lane 1 decreases to its minimum value. This value is determined using the Pythagorean theorem applied to the hatched triangle shown in the diagram:

$$y_{min\_lane1} = \sqrt{R_{eff}^2 - \left(\frac{\Delta L}{2}\right)^2} \quad (12)$$

Determination of the "Farthest Point" of Lane 2 (The Peak)

The vehicle in Lane 2 is deployed in a staggered configuration, meaning that the stopping positions of Lane 2 are longitudinally offset by exactly $\frac{\Delta L}{2}$ relative to Lane 1. Consequently, when Lane 1 encounters the most disadvantageous "gap" (the valley), Lane 2 is simultaneously positioned at its most favorable state - aligned exactly with the rotation center of the working platform. This geometric complementarity serves as the fundamental justification for selecting the two-sided staggered stopping strategy in this thesis.

At this specific position,

$$y_{max\_lane2} = R_{eff} \quad (13)$$

Coverage Constraint (Condition for Coverage)

To ensure the elimination of any gaps on the bridge underside or the formation of "dead zones," the combined reach of the "weakest point" of Lane 1 and the "strongest point" of Lane 2 must be greater than or equal to the bridge width (B), incorporating a safety margin (B_{margin}).

The coverage constraint is established as follows:

$$y_{min\_lane1} + y_{max\_lane2} \geq B + B_{margin} \quad (14)$$

Geometric Equation Formulation

Substituting formulas (12) and (13) into the coverage constraint, we obtain the governing equation for the critical state:

$$\sqrt{R_{eff}^2 - \left(\frac{\Delta L}{2}\right)^2} + R_{eff} = B + B_{margin} \quad (15)$$

Solving the Equation for the Step Size ΔL

Solving Equation (15), we obtain the optimal step size formula:"

$$\Delta L_{opt} = 2 \times \sqrt{R_{eff}^2 - (B - R_{eff} + B_{margin})^2} \quad (16)$$

The derived formula allows for a significant expansion of the vehicle's step size while guaranteeing absolute geometric coverage, utilizing the "peak-to-valley" compensation mechanism between the two staggered scanning lanes.

To provide a scientific basis for the manufacturer in publishing technical specifications, the study determines the maximum bridge width B_{max} that the device can inspect based on the current manipulator configuration (R_{eff} = 6.0 m).

Theoretical Limit

Geometrically, the maximum width where the two manipulator arms from opposite sides can just touch each other (assuming zero overlap and zero step size) is twice the working radius:

$$B_{theoretical} = 2R_{eff} = 12\ m \quad (17)$$

However, at this limit, the device cannot move longitudinally (step size $\Delta L = 0$), and there is no safety tolerance for control errors. Therefore, this is only an ideal reference figure.

Practical Limit and Recommendations

In practical operating conditions, it is mandatory to maintain a safety overlap margin B_{margin} to compensate for positioning errors and structural vibrations. Applying the established optimization formula, the condition for the problem to have a feasible solution (i.e., step size $\Delta L \geq 0$) is:

$$\Delta L_{opt} = 2\sqrt{R_{eff}^2 - (B_{max} - R_{eff} + B_{margin})^2} \geq 0 \quad (18)$$

At the limit state (step size approaches 0), we have the equilibrium equation:

$$R_{eff}^2 - (B_{max} - R_{eff} + B_{margin})^2 = 0$$
$$\rightarrow B_{max} = 2R_{eff} - B_{margin} \quad (19)$$

With the recommended safety parameter of

$B_{margin} = 0.5m$, the maximum allowable bridge width is:

$$B_{max} = 2 \times 6.0 - 0.5 = 11.5 \text{ m} \quad (20)$$

The device with the current manipulator configuration ($R_{eff} = 6m$) operates most effectively for bridges with widths B ≤ $11.5m$. Within this range, the optimization algorithm ensures 100% coverage of the bridge underside with a minimized number of vehicle stops. For bridge structures with widths B > 11.5m, the device will encounter "dead zones" (blind spots) along the bridge centerline.

Based on the workspace analysis and the step size optimization formulas established previously, this study develops a quantitative computational algorithm to accurately determine the vehicle's stopping positions. The algorithm is designed using the analytical geometry method to automate the operational planning process, ensuring the simultaneous satisfaction of two objectives: 100% coverage of the bridge underside and optimization (minimization) of the number of movement steps. The specific implementation procedure consists of the following 6 steps:

Step 1: Data Initialization

Set up the input parameters for the problem:

Input bridge parameters: Bridge length: L; Bridge width: B;

Input equipment parameters: Effective working radius: R_{eff};

Safety parameter: Safety overlap margin: B_{margin};

Safety clearance at both bridge ends L_{margin}.

where $L_{margins}$ represents the total clearance distance at both ends of the bridge span. The vehicle cannot stop directly at the bridge edge; a safety distance is required to allow manipulator deployment and to prevent collisions with the abutment.

In this study, the clearance distance is assumed as $L_{margins} = 1.0$ m corresponding to a safety clearance of 0.5 m at each end of the bridge.

Step 2: Feasibility Domain Analysis

If $B > B_{max} = 2(R_{eff} - B_{margin})$ bthen the problem has no feasible solution. The algorithm terminates and issues a warning.

If $B \leq B_{max} = 2(R_{eff} - B_{margin})$ the algorithm proceeds to the next step.

Step 3: Calculation of Maximum Step Size

Using the geometric optimization formula for the staggered layout strategy, the optimal step size is computed as

$$\Delta L_{opt} = 2 \times \sqrt{R_{eff}^2 - (B - R_{eff} + B_{margin})^2}$$

Step 4: Integer Discretization

Since the number of vehicle stopping positions must be an integer, a ceiling operation is applied:

$$n_{intervals} = \left\lceil \frac{L - L_{margins}}{\Delta L_{opt}} \right\rceil \quad (21)$$

The number of vehicle stops (n_{stops}) equals the number of intervals plus 1:

$$n_{stops} = n_{intervals} + 1 \quad (22)$$

Step 5: Step Size Redistribution (Recalculation)

To ensure that stopping positions are uniformly distributed along the entire bridge length, the actual step size ΔL_{real} is recalculated by dividing the working length by the determined integer number of intervals:

$$\Delta L_{real} = \frac{L - L_{margins}}{n_{intervals}} \quad (23)$$

The value of ΔL_{real} is always less than or equal to ΔL_{opt}, ensuring that safety conditions are strictly satisfied and even improved compared to theoretical calculations.

Step 6: Coordinate Determination and Result Output

Determine the stopping position vectors for the two travel lanes. The "Staggered Scanning" strategy is implemented by creating a phase offset between Lane 1 and Lane 2.

-Lane 1

$$P_1 = \{ p_{1,i} \mid p_{1,i} = \frac{L_{margins}}{2} + (i-1)\Delta L_{real}, \quad i = 1 \dots n_{stops} \} \quad (24)$$

The starting position of Lane 2 is shifted by $\frac{\Delta L_{real}}{2}$ relative to Lane 1 to fill the geometric dead zones.

$$P_2 = \{ p_{2,i} \mid p_{2,i} = p_{1,i} + \frac{\Delta L_{real}}{2}, i = 1 \dots n_{stops} \} \quad (25)$$

End of Algorithm

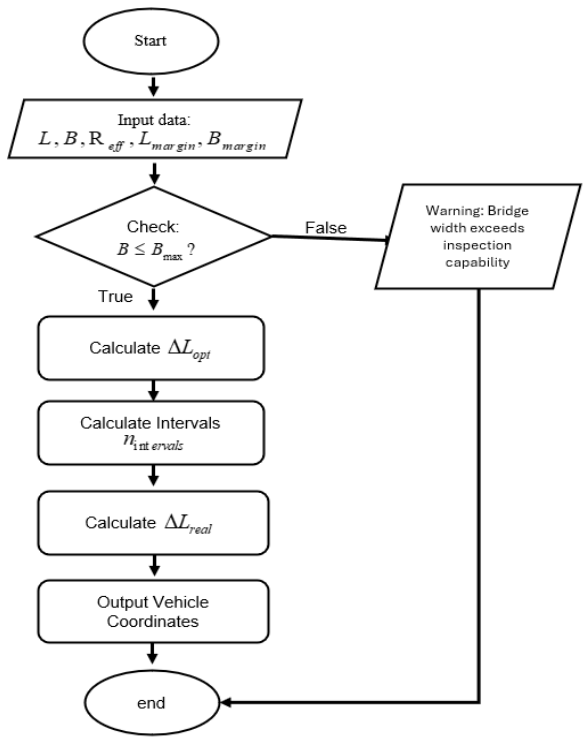

Figure 10. *Flowchart of the optimal vehicle positioning algorithm*

A schematic diagram illustrating the workflow of the optimization algorithm based on the analytical geometry method is shown in Figure 10.

3.3. Simulation Results and Discussion

To verify the validity and evaluate the practical effectiveness of the proposed algorithm, the study conducts a numerical simulation for a typical bridge span case with dimensions $L = 32m$ and $B = 10m$. Given the device's input parameters of $R_{eff} = 6.0m$ and a safety margin of $B_{margin} = 0.5m$, $L_{margin} = 1m$, the resulting optimal distribution of vehicle stopping positions is determined as follows:

For a typical 32m span bridge with a 10m width, the algorithm identifies an optimal real step size of Δ Lreal = 7.75 m. The entire inspection task is completed with only 9 vehicle stops (5 in Lane 1 and 4 in Lane 2). Visual simulations confirm that the staggered compensation mechanism successfully eliminates all geometric dead zones, ensuring 100% accessibility to the underside. Under the current configuration (R_{eff} = 6.0 m), the device operates effectively for bridges with widths up to 11.5 m.

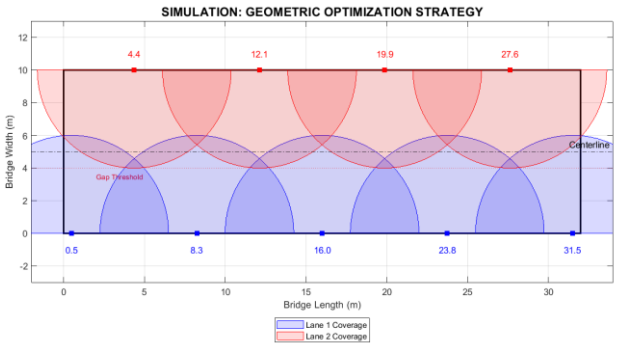

Figure 11. *Simulation results of the optimal scanning strategy for a typical bridge span ($L = 32m, B = 10m$)*

4. Conclusions and recommendations

The study has successfully established a precise kinematic model of the device, serving as the fundamental basis for solving the positioning optimization problem. Calculation and simulation results confirm that the device (with $R_{eff} = 6.0$m) operates effectively on bridges with widths up to B $\leq$ 11.5m, significantly minimizing the number of vehicle stops and reducing inspection time.

Based on these findings, the authors recommend: Integrating the optimization algorithm into the central controller to automate the operation process; and improving the hardware by developing lateral sliding mechanisms or extending telescopic arms to accommodate bridges exceeding the theoretical width limits.

Acknowledgements: This study is funded by University of Transport Technology (UTT), Military Technical Academy (MTA), and Institute of Transportation Science and Technology (ITST)

REFERENCES

[1] B. T. Thanh, T. D. Nhiem, N. V. Minh, and N. H. Thuan, *Exploitation and Inspection of Bridges*, Hanoi, Vietnam: Transp. Publishing House, 2017.

[2] Z. Wang, B. He, K. Y. Zhou, L. Liu, and C. Zhang, "Design and Implementation of a Cable Inspection Robot for Cable-Stayed Bridges," *Robotica*, vol. 39, no. 8, pp. 1417–1433, 2021. https://doi.org/10.1017/S0263574720001253

[3] L. Q. Thuy *et al*., "*Research, design, and manufacturing of equipment for inspection, testing, repair, and upgrading of under-bridge structures"*, research project report, Ministry of Transport, Vietnam, DT203028, 2020.

[4] B. H. Dung, N. T. Son, U. H. Billah, L. Chuong, A. Tavakkoli, and L. M. Hung, "Control Framework for a Hybrid-steel Bridge Inspection Robot", in *Proc. IEEE/RSJ Int. Conf. Intell. Robots Syst. (IROS)*, Las Vegas, NV, USA, 2020, pp. 2585–2591.

[5] S. Fu, D. Yang, Z. Mei, and W. Zheng, "Progress in Construction Robot Path-Planning Algorithms: Review"*, Appl. Sci.*, vol. 15, no. 3, p. 1165, 2025. https://doi.org/10.3390/app15031165

[6] K. Nakata, K. Umemoto, K. Kaneko, and R. Fujisawa, "Development And Operation Of Wire Movement Type Bridge Inspection Robot System ARANEUS", *Kalpa Publ. Eng.*, vol. 3, pp. 168–174, 2020. https://doi.org/10.29007/zw9k

[7] P. Kim and J. Youn, "Drone Path Planning for Bridge Substructure Inspection Considering GNSS Signal Shadowing," *Drones*, vol. 9, no. 2, Art. no. 124, 2025. https://doi.org/10.3390/drones9020124

[8] T. Q. Thanh and P. Q. Dung, *Lifting Machines and Equipment*, Hanoi, Vietnam: Sci. and Technol. Publishing House, 2004.

[9] N. V. Khang, *Multibody System Dynamics*, 2nd edition, Hanoi, Vietnam: Sci. and Technol. Publishing House, 2017.

[10] M. W. Spong, S. Hutchinson, and M. Vidyasagar, *Robot Modeling and Control*, 2nd edition. Hoboken, NJ, USA: Wiley, 2020.

[11] B. V. Tram, "*Dynamic analysis of rotary-percussive drilling equipment mounted on excavators for medium and small-scale tunnel construction*", Doctoral dissertation, Military Technical Academy, Hanoi, Vietnam, 2019.

[12] M. W. Spong, S. Hutchinson, and M. Vidyasagar, *Robot modeling and control*, Wiley, Hoboken, 2020.

[13] D. T. Quoc and L. T. Dung, " Kinematics and singularity analysis of 3 degree-of-freedom planar parallel robotic manipulators", *The University of Danang - Journal of Science and Technology*, Vol 5, No 114.1, pp 76-80, 2017.

[14] L. T. Hue and N. P. T. Anh, "Planning the optimal trajectory for a robotic manipulator using genetic algorithm", *The University of Danang - Journal of Science and Technology*, Vol 20, no 4, pp 74-79, 2022.

[15] L. T. Hieu *et al*., "Velocity kinematic controller design for an industrial manipulator with a palletizing configuration", *The University of Danang - Journal of Science and Technology,* Vol. 23, No. 9A, pp 70-74, 2025.